

3D inversion of frequency-domain controlled source electromagnetic data for hydraulic fracturing fluid imaging with the effect of steel casings

Ying Hu¹, and Dikun Yang¹

¹ Department of Earth and Space Sciences, Southern University of Science and Technology

SUMMARY

Proper utilization of steel casings in the oil and gas development can amplify surface controlled source electromagnetic (CSEM) responses arising from small conductivity perturbations in the reservoir. This work established the capability of recovering the 3D distribution of injected fluid during the operation of fracturing with the presence of arbitrarily complex steel casings. Our approach incorporates steel casings into the conductivity model through the use of edge conductivity, a newly proposed physical property parameter defined as the product of the intrinsic conductivity and cross-sectional area of casing pipe. By assigning edge conductivities to mesh edges and taking them into account in the finite volume formulation, we efficiently capture the effects of casings without any mesh refinement. The inverse problem is solved by the Gauss-Newton method with an objective function containing the smoothness constraints on models. Through a synthetic example involving realistic host rock resistivities and horizontal wells, we show that our algorithm can successfully map the directional flow of injected fluid flow using the top-casing source and electric field data acquired near the well head.

Keywords: 3D Inversion, CSEM, Steel casing, Hydraulic fracturing

INTRODUCTION

Electromagnetic methods are widely applied in assessing reservoir conditions, stimulating reservoir volume, and monitoring fracturing fluid migration during hydraulic fracturing operations (Commer et al., 2020; Hoversten and Schwarzbach, 2021; Li and Yang, 2021).

Hydraulic fracturing imaging models typically involve steel casings with minimal radii and thicknesses significantly smaller than the overall size of rock formations. The presence of steel casings can generate distortion in CSEM data, necessitating sophisticated data processing techniques. However, numerous studies have acknowledged the positive contribution of steel casings to electromagnetic methods: they can enhance observed signals on the surface, especially for deep reservoirs with highly conductive hydraulic fracturing fluids (Weiss et al., 2016; Heagy and Oldenburg, 2022; Hu et al., 2022).

A number of inversion approaches for hydraulic fracturing fluid have been proposed. Some of them have focused on optimizing survey configurations to avoid simulating steel casings or to enhance signal amplitudes (Grayver et al., 2014; Um et al., 2020; Hoversten and Schwarzbach, 2021). Others have simplified hydraulic fracturing fluids into two-dimensional octagonal or non-rectangular shapes (Zhang et al., 2020; Li and Yang, 2021). There are also studies relying on the location data, enforcing robust spatial constraints, or incorporating additional information during the inversion process. (Commer et al., 2020; Noh et al., 2020).

In this study, we develop the 3D simulation algorithm that does not only take cell conductivities defined in mesh cells but also allows assigning edge conductivities to the mesh edges to present steel casings. During the inversion process, we recover the electrical conductivity of the region of interest while fixing the edge conductivities of the casings as a prior. By integrating the edge conductivity modeling into the 3D inversion, we enhance the accuracy of subsurface fluid imaging, and assist the monitoring of the fluid injection.

METHODS

Forward Modeling

Our inversion is based on a 3D-modified finite-volume electromagnetic modeling algorithm (Hu et al., 2022). The governing partial differential equation for the total electric field in CSEM applications is obtained by eliminating the magnetic field in the Maxwell's equations:

$$\nabla \times \nabla \times \mathbf{E} + i\omega\mu\sigma\mathbf{E} = -i\omega\mu\mathbf{J}_s, \quad (1)$$

where \mathbf{E} represents the electric field, ω is the angular frequency, μ is the magnetic permeability, σ and ϵ represent the electrical conductivity and permittivity, and \mathbf{J}_s is the external current source.

In Figure 1(a), the yellow-highlighted region represents a control volume that contains four conductive rectangular prisms oriented along the y-direction. The red-highlighted solid line represents a section of steel casing coinciding

with an edge of the control volume. Applying Stokes' theorem to equation (1), we derive

$$\oint_{\Gamma} \mathbf{H} \cdot d\Gamma = \iint_S \nabla \times \mathbf{H} \cdot d\mathbf{S} = \iint_S (\sigma \mathbf{E} + \mathbf{J}_s) \cdot d\mathbf{S} \quad (2)$$

Considering the relatively small cross-sectional area of the steel casing, we can neglect its exact geometric details. Instead, we can use the concept of edge conductivity, which is the product of the cross-sectional area and electrical conductivity, and then readily compute the average electrical conductivity by using edge conductivity (Hu et al., 2022). Similar simulation strategies have also been developed for the finite element method (Weiss, 2017).

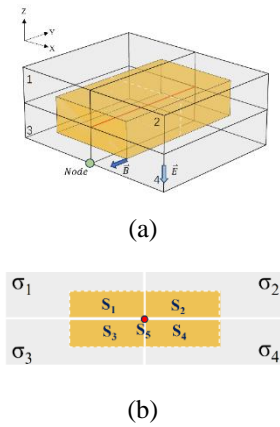


Figure 1: Modified finite volume method in a Cartesian, rectangular mesh. (a) A control volume defined around an edge in the y-direction. (b) Calculation of the averaged conductivity.

Our algorithm uses the rectilinear mesh. To simulate arbitrary well paths in 3D space, our code approximate well paths using the surrounding mesh edges. The conductance of a casing segments not directly on mesh edges is redistributed to the nearest eight edges using orthogonal decomposition and tri-linear interpolation, with contributions from neighboring casing segments summed up for the total edge conductivity calculation.

We carry out two casing-in-whole-space simulations, one original and the other as the rotated version of the original (Fig. 2) to validate the algorithm for arbitrary well paths. The background conductivity and the relative location information in the two simulations are identical. The findings depicted in Fig. 3 validate the accuracy of the algorithm. The rotation of the original configuration results in the casing not aligned perfectly with the grid. In both configurations, the amplitude and phase consistently follow a specific pattern. At the observation offsets beyond 125 meters from the steel casing, the relative differences are mostly within 8% for the amplitude and phase.

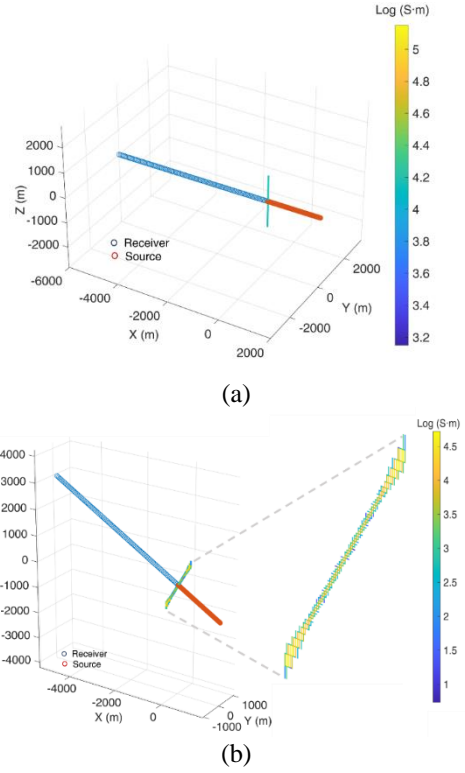


Figure 2: Tilted well test. (a) The original and (b) rotated configuration. The steel casing is represented by non-zero edge conductivities on the color-coded mesh edges. The source is a grounded wire connecting the mid-point of a finite-length casing and a remote point.

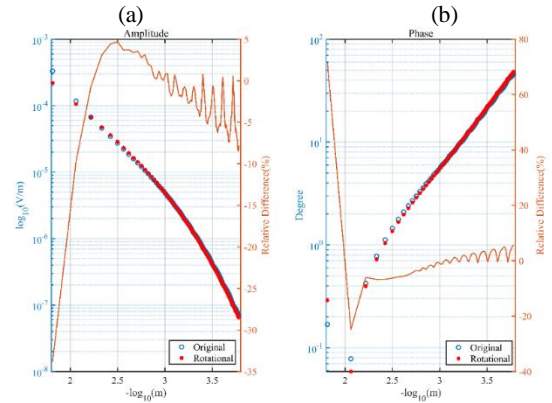


Figure 3: Electric field data at receivers in Figure 2 at 1 Hz. (a) Amplitude; (b) Phase angle.

Inverse modeling algorithm with steel casings

Our inversion relies on a universal frequency-domain electromagnetic inversion framework with the objective function as follows

$$\phi(m) = \frac{1}{2} \|W_d [F(m) - d_{obs}]\|_2^2 + \frac{\beta}{2} \|W_m (m - m_{ref})\|_2^2 \quad (3)$$

where W_d is a data-weighting matrix; d_{obs} and $F(m)$ are observed and predicted data, respectively; W_m is the model weighting matrix; m_{ref} is the reference model containing a variety of prior geological information; and $\frac{\beta}{2}$ is a regularization parameter. In our algorithm, the model in equation (3) is a stack of the cell, face, and edge conductivity model vectors. The smoothness constraint are applied to the face and edge conductivity parameters if they are to be recovered in the inversion

$$W_m = \begin{bmatrix} W_c & & \\ & W_f & \\ & & W_e \end{bmatrix}, m_{ref} = \begin{bmatrix} m_c \\ m_f \\ m_e \end{bmatrix}. \quad (4)$$

We employ a Gauss-Newton approach to solve the optimization problem that minimizes equation (3). The model updates are calculated by iteratively solving

$$[\text{Re}\{J^H W_d^H W_d J\} + \beta W_m^T W_m] \delta m = -[\text{Re}\{J^H W_d^H W_d [F(m) - d_{obs}]\} + \beta W_m^T W_m (m - m_{ref})]. \quad (5)$$

Here, δm is a model update vector, and $J \in X^{N_d \times N_m}$ is the weighted sensitivity matrix that represents the partial derivatives of the data to the model parameters. The matrix on the left-hand side corresponds to the regularized approximate Hessian, while the right side represents the negative gradient indicating the descent direction.

In some cases, it is possible to directly solve and store the sensitivity matrix, a method referred to as explicit solving. However, storing the sensitivity matrix can consume significant memory resources when dealing with a large volume of data or a high number of model parameters. The limitation becomes especially relevant when considering frequency-domain 3D inversion with steel casing, where the model parameters include the cell, face, and edge elements. As a result, this paper opts for an implicit approach to compute the sensitivity matrix for matrix-vector product operation required by equation (5):

$$J \cdot \delta m = Q A^{-1} \text{diag}(E) \cdot A_{m2e} \cdot \text{diag}(m) \cdot \delta m, \quad (6)$$

$$J^H \cdot \delta m = \text{diag}(m) \cdot A_{m2e}^T \cdot \text{diag}(E) \cdot (A^{-1})^H \cdot Q^T \cdot \delta m, \quad (7)$$

where \mathbf{A} represents the forward operator and \mathbf{Q} represents the data projection matrix. A sparse matrix A_{m2e} can map conductivity values from cell centers to edges. We establish two categories of model parameters for the inversion process: active and inactive. All model parameters are utilized in the forward modeling, but updates are exclusively applied to those designated as active during the inversion.

NUMERICAL EXPERIMENTS

We validate our computational framework of inversion using a synthetic fracturing monitoring example. Specifically, we design simulations involving three steel-

cased wells positioned at a depth of 1900 m within a layered background model. The separation between the vertical wells is 50 m, while for the horizontal well is 350 m. The central wellhead is directly connected to an electrical current source of 1 A at 0.01 Hz, with a remote electrode situated 2 km away. To capture the complete electrical field pattern, we employ a uniform measurement grid around the central wellhead, covering a 300×300 m area with measurements every 25 m (Fig. 4(a)).

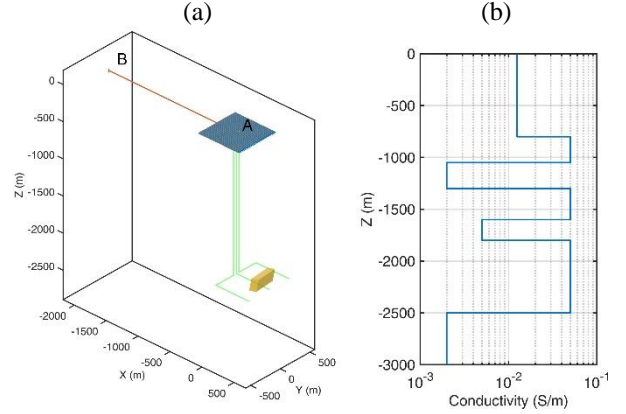


Figure 4: Setup of the synthetic inversion example. (a) The three steel-cased wells, source electrodes, receivers, and injected fluid; (b) Layered background conductivity model.

The injected fluid was represented by a conductive block measuring 150 × 300 × 200 m, with a conductivity of 1 S/m. This block is asymmetrically distributed with respect to the middle well, representing a flow towards the +y direction. The synthetic data generated through forward modeling serve as the observed data for the subsequent inversion. In the inversion, a constant edge conductivity value of 150,000 S·m for all well sections is assumed.

To accurately define the active region for recovery of fluid's cell conductivity, the information of perforation position is used as a prior. Such information constrains active cells within a reasonable region: 0 to 500 m in the x-direction, -500 to 500 m in the y-direction, and -1800 to -2200 m in the z-direction.

Our inversion results successfully recovered the preferential fluid flow towards the +y direction (Fig. 5). This phenomenon was attributed to the enhanced sensitivity of our survey to horizontal fluid movements, a consequence of the parallel configuration of the wells. The blurred boundaries in our inversion results were anticipated outcomes of the smoothness constraint. The synthetic example indicates the effectiveness of our approach in capturing the underlying fluid dynamics. The amplitude and phase of the surface data have also been well-fitted (Fig. 6).

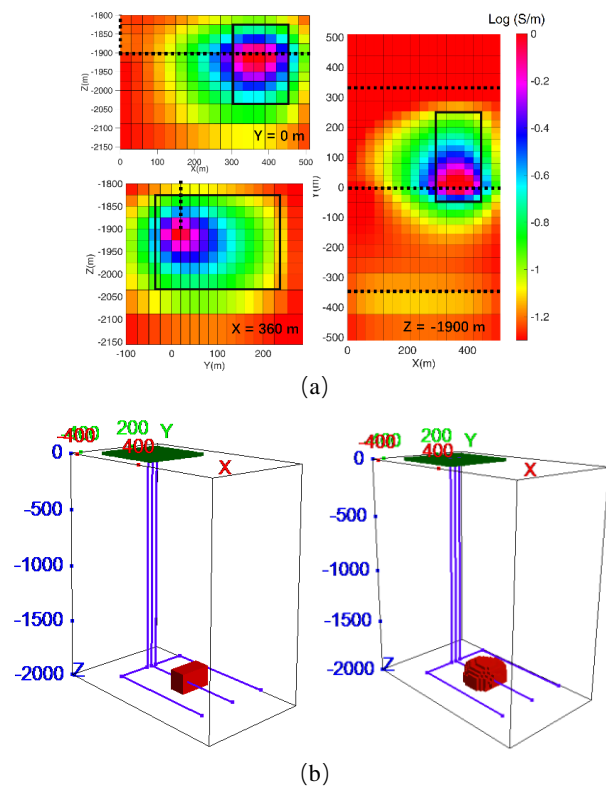


Figure 5: Inversion results of the hydraulic fracturing fluid. (a) The model is sliced at $Y = 0$ m, $X = 360$ m, and $Z = -1900$ m. The solid black lines represent the true fluid model and the dotted lines indicate the well. (b) 3D views of the true model (left) and recovered model (right) with the steel casings.

CONCLUSION

Our study established the capability of 3D CSEM inversion in the presence of steel casings. We address the complexity and cost associated with rigorously modeling of steel casing in CSEM inversions by incorporating edge conductivity into the model. Our approach eliminates the need for intricate mesh refinement, and updates only specific model elements exclusively during the inversion, simplifying the overall computational procedure. These strategies ensure that our algorithm is computationally efficient and cost-effective.

Our proposed algorithm stands out for its simplicity, speed, and practical implementation. It does not demand extensive computational resources or intricate mesh adjustments, making it a viable choice for real-world applications. The effectiveness of our approach is demonstrated through a practical example of fracturing monitoring, in which the directional flow of injected fluid is recovered as a 3D conductivity model by using a top-casing source and surface receivers.

ACKNOWLEDGMENTS

This work was funded by the National Natural Science Foundation of China (no. 41974087). The computational work was supported by Center for Computational Science and Engineering at Southern University of Science and Technology.

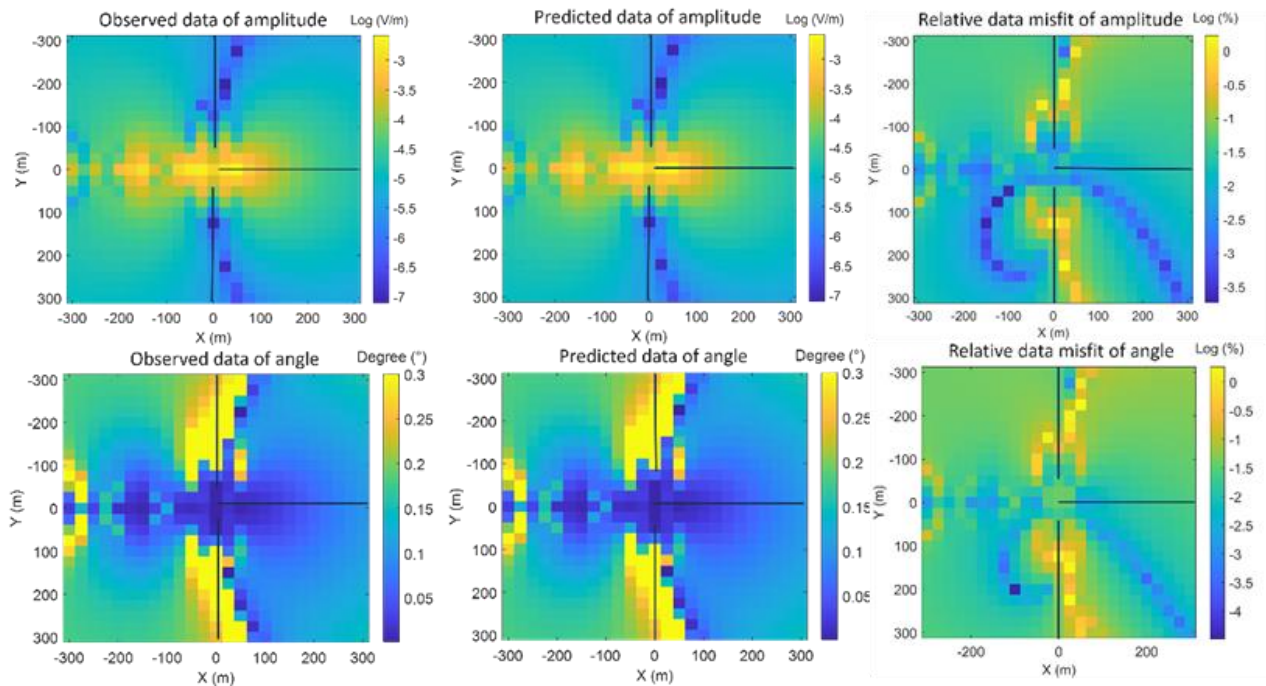


Figure 6: Data fitting of the inversion. The first row is for the amplitude, and the second row for the phase angle. The solid black lines represent the projection of the casings. A top-casing source is connected to the middle wellhead.

REFERENCES

- Commer, M., S. Finsterle, and G. Hoversten, 2020, Three-dimensional fracture continuum characterization aided by surface time-domain electromagnetics and hydrogeophysical joint inversion—proof-of-concept: *Computational Geosciences*, 24, 1–15.
- Grayver, A. V., R. Streich, and O. Ritter, 2014, 3D inversion and resolution analysis of land-based CSEM data from the Ketzin CO₂ storage formation: *Geophysics*, 79, 820–830.
- Heagy, L. J., and D. W. Oldenburg, 2022, Electrical and electromagnetic responses over steel-cased wells: *The Leading Edge*, 41, 83–92.
- Hoversten, G. M., and C. Schwarzbach, 2021, Monitoring hydraulic fracture volume using borehole to surface electromagnetic and conductive proppant: *GEOPHYSICS*, 86, E93–E109.
- Hu, Y., D. Yang, Y. Li, Z. Wang, and Y. Lu, 2022, 3-D Numerical Study on Controlled Source Electromagnetic Monitoring of Hydraulic Fracturing Fluid With the Effect of Steel-Cased Wells: *IEEE Transactions on Geoscience and Remote Sensing*, 60, 1–10.
- Li, Y., and D. Yang, 2021, Electrical imaging of hydraulic fracturing fluid using steel-cased wells and a deep-learning method: *GEOPHYSICS*, 86, E315–E332.
- Noh, K., K. Ha Lee, S. Oh, S. Jee Seol, and J. Byun, 2020, Location-based parameterization of controlled-source electromagnetic data inversion for the monitoring of hydraulic fracturing with magnetically enhanced proppants: *GEOPHYSICS*, 85, E27–E39.
- Um, E. S., J. Kim, and M. Wilt, 2020, 3D borehole-to-surface and surface electromagnetic modeling and inversion in the presence of steel infrastructure: *GEOPHYSICS*, 85, E139–E152.
- Weiss, C. J., 2017, Finite-element analysis for model parameters distributed on a hierarchy of geometric simplices: *GEOPHYSICS*, 82, E155–E167.
- Weiss, C. J., D. F. Aldridge, H. A. Knox, K. A. Schramm, and L. C. Bartel, 2016, The direct-current response of electrically conducting fractures excited by a grounded current source: *GEOPHYSICS*, 81, E201–E210.
- Wilt, M. J., E. S. Um, E. Nichols, C. J. Weiss, G. Nieuwenhuis, and K. MacLennan, 2020, Casing integrity mapping using top-casing electrodes and surface-based electromagnetic fields: *GEOPHYSICS*, 85, E1–E13.
- Zhang, R., Q. Sun, X. Zhang, L. Cui, Z. Wu, K. Chen, D. Wang, and Q. H. Liu, 2020, Imaging Hydraulic Fractures Under Energized Steel Casing by Convolutional Neural Networks: *IEEE Transactions on Geoscience and Remote Sensing*, 58, 8831–8839.